HHS Public Access

Author manuscript

Cancer Res. Author manuscript; available in PMC 2017 July 29.

Published in final edited form as:

Cancer Res. 2017 July 15; 77(14): 3931–3941. doi:10.1158/0008-5472.CAN-17-0299.

Non-invasive Interrogation of DLL3 Expression in Metastatic Small Cell Lung Cancer

Sai Kiran Sharma[1,2], **Jacob Pourat**[1,2], **Dalya Abdel-Atti**[1,2], **Sean D. Carlin**[1,2], **Alessandra Piersigilli**[3], **Alexander J. Bankovich**[6], **Eric E. Gardner**[2], **Omar Hamdy**[6], **Kumiko Isse**[6], **Sheila Bheddah**[6], **Joseph Sandoval**[6], **Kristen M. Cunanan**[7], **Eric B. Johansen**[6], **Viola Allaj**[2,4], **Vikram Sisodiya**[6], **David Liu**[6], **Brian M. Zeglis**[1,5,8,9], **Charles M. Rudin**[2,4,5], **Scott J. Dylla**[6], **John T. Poirier**[2,4], and **Jason S. Lewis**[1,2,5]

[1]Department of Radiology, Memorial Sloan Kettering Cancer Center, New York, NY, USA

[2]Program in Molecular Pharmacology, Memorial Sloan Kettering Cancer Center, New York, NY, USA

[3]Tri-Institutional Laboratory of Comparative Pathology, Memorial Sloan Kettering Cancer Center, Weill Cornell Medical College, and The Rockefeller University, NY, USA

[4]Department of Medicine, Memorial Sloan Kettering Cancer Center, New York, NY, USA

[5]Weill Cornell Medical College, New York, NY, USA

[6]Stemcentrx, Inc., South San Francisco, CA, USA

[7]Department of Epidemiology and Biostatistics, Memorial Sloan Kettering Cancer Center, New York, NY, USA

[8]Department of Chemistry, Hunter College and the Graduate Center of the City University of New York, New York, NY, USA

[9]Ph.D. Program in Chemistry, the Graduate Center of the City University of New York, New York, NY, USA

Abstract

The Notch ligand DLL3 has emerged as a novel therapeutic target expressed in small cell lung cancer (SCLC) and high-grade neuroendocrine carcinomas. Rovalpituzumab teserine (Rova-T™; SC16LD6.5) is a first-in-class DLL3-targeted antibody-drug conjugate with encouraging initial safety and efficacy profiles in SCLC in the clinic. Here we demonstrate that tumor expression of DLL3, though orders of magnitude lower in surface protein expression than typical oncology targets of immunoPET, can serve as an imaging biomarker for SCLC. We developed 89Zr-labeled SC16 antibody as a companion diagnostic agent to facilitate selection of patients for treatment with Rova-T based on a non-invasive interrogation of the in vivo status of DLL3 expression using PET imaging. Despite low cell-surface abundance of DLL3, immunoPET imaging with 89Zr-labeled SC16 antibody enabled delineation of subcutaneous and orthotopic SCLC tumor

*Co-corresponding Authors: Jason S. Lewis; Memorial Sloan Kettering Cancer Center, 1275 York Avenue, New York, NY 10065; Phone: 646-888-3039, Fax: 646-888-3059; lewisj2@mskcc.org. John T. Poirier; Memorial Sloan Kettering Cancer Center, 417 East 68th Street, New York, NY 10065; Phone: 646-888-3588, Fax: 646-422-0247; poirierj@mskcc.org.

xenografts as well as distant organ metastases with high sensitivity. Uptake of the radiotracer in tumors was concordant with levels of DLL3 expression and, most notably, DLL3 immunoPET yielded rank-order correlation for response to SC16LD6.5 therapy in SCLC patient-derived xenograft models.

Keywords

Small cell lung cancer; Delta-like protein 3; DLL3; immunoPET

INTRODUCTION

Small cell lung cancer (SCLC) is an extremely lethal form of lung cancer that accounts for 16% of all lung cancer cases diagnosed annually in the United States (1, 2). The majority of SCLC cases are metastatic at the time of diagnosis, necessitating effective systemic therapies (3). The standard of care for extensive stage SCLC consists of a combination of the cytotoxic agents cisplatin or carboplatin with etoposide (4). While patients respond to these therapies, they often relapse shortly after the cessation of treatment, accounting in part for a dismal 5-year survival rate of 2% (5). These outcomes have not meaningfully improved in more than 3 decades (6). There are no FDA-approved targeted therapies for SCLC, and no approved therapies of any kind beyond topotecan in the second line. There is a desperate need for novel systemic therapies as well as diagnostic approaches to direct these therapies to the patients most likely to benefit from them.

We recently reported that delta-like protein 3 (*DLL3*) is a highly tumor-selective cell surface protein expressed in high-grade neuroendocrine lung tumors including SCLC (7). DLL3 is an inhibitory ligand of the Notch signaling pathway that is normally expressed exclusively on intracellular membranes, including those of the Golgi apparatus (8). However, marked induction of *DLL3* expression in SCLC results in localization to the cell surface: this together with the absence of detectable cell surface DLL3 in non-malignant cells opens a new window of opportunity for tumor-cell specific therapy. Of particular relevance to SCLC, DLL3 is implicated in the regulation of clonogenic and tumorigenic capacity (7). Exceptionally high clonogenic capacity, early metastatic spread, and rapid tumor repopulation after exposure to chemotherapy are hallmark features of SCLC (9).

Rovalpituzumab teserine (Rova-T; SC16LD6.5) is a DLL3-targeted antibody-drug conjugate (ADC) comprising a humanized anti-DLL3 monoclonal antibody [rovalpituzumab (SC16)], a cleavable dipeptide linker, and a cell cycle-independent pyrrolobenzodiazepine (PBD; D6.5) toxin (7, 10). SC16LD6.5 was reported to selectively target DLL3-expressing cells compared to an isotype-matched control antibody formulation. Treatment with the DLL3-targeted ADC completely and durably eradicated SCLC patient-derived xenografts (PDX) expressing high levels of DLL3 in a variety of preclinical models including those resistant to cisplatin and etoposide. Furthermore, a recently completed first-in-human phase I trial of Rova-T in patients with relapsed SCLC demonstrated encouraging clinical outcomes (11). Among the 67% of patients with > 50% of cells expressing DLL3 ($DLL3^{Hi}$), a confirmed objective response rate of 39% and confirmed disease control rate of 89% were observed

(11). Importantly, *all* patients with confirmed objective responses by investigator assessment were DLL3^{Hi} by immunohistochemistry (IHC). This early clinical experience highlights the significance of DLL3 assessment as a predictive biomarker for DLL3-targeted agents.

Despite these encouraging early clinical results, IHC suffers from several limitations that may reduce its effectiveness as a clinical diagnostic for DLL3-targeted therapies. These limitations include (a) the lack of contemporaneous tissue biopsy, an especially acute problem in aggressive carcinomas like SCLC, where multiple biopsies are rarely performed; (b) the sampling bias caused by intratumoral heterogeneity or heterogeneity between the primary tumor and metastases; and (c) the inherently high false-negative rate of histopathological assessment. Such limitations have led to the recent emergence and application of immuno-positron emission tomography (immunoPET) as a more reliable approach for the noninvasive evaluation of tumor-associated antigen expression *in vivo* (12). ImmunoPET may reflect physiologic drug binding more accurately than IHC of tumor sections *ex vivo* due to factors such as high intratumoral oncotic and hydrostatic pressures and variable perfusion that can limit delivery of antibody-based therapeutics. An increasing number of immunoPET strategies are now being translated into oncologic imaging protocols for patient evaluation prior to treatment with antibody-based targeted therapeutics (13–15). This trend can be attributed to the exquisite specificity of antibodies for tumor-associated molecular targets/antigens combined with the sensitivity and quantitative nature of PET (16).

We envisaged that a real-time, noninvasive, and quantitative approach to evaluate the *in vivo* status of DLL3 expression in patient tumors would have immediate clinical utility in the context of DLL3-targeted therapies. To this end, we have developed a ^{89}Zr-labeled, DLL3-targeted immunoconjugate leveraging the humanized antibody, SC16, to serve as a companion diagnostic immunoPET agent in neuroendocrine carcinoma patients. Here we report the PET imaging performance of this agent in preclinical mouse models of SCLC.

MATERIALS AND METHODS

Gene expression analysis

Gene expression data from 2,712 normal samples representing 55 different organs was downloaded from the Genotype-Tissue Expression (GTEx) project (release V4) as reads per kilobase of transcript per million mapped reads (RPKM). Raw RNAseq reads from primary SCLC and normal lung were aligned to the human reference genome GRCh37 with TopHat v1.1.4 assisted by GENCODE transcript model v18. RPKM values were calculated using RNA-SeQC v1.1.8 run in strict mode, consistent with published analysis methods for GTEx release V4. Since both data sets include samples of normal lung, it was possible to apply batch effect correction prior to further analysis (17).

Robust Multi-array Average (RMA) and quartile normalized gene expression microarray data for 1,037 cancer cell lines was downloaded from the Cancer Cell Line Encyclopedia (CCLE). Two SCLC cell lines, H82 and H69, were identified as being representative of median and low-*DLL3* expression, respectively. A gene expression cutoff was set for this analysis using the approach of Zilliox et al. (18). A549, a non-small cell lung cancer line exhibiting DLL3 expression below the cutoff, was used as a negative control in the *in vitro*

and *in vivo* experiments to validate the DLL3-specific tumor uptake of the SC16-based radioimmunoconjugates. All downstream analysis and figure generation was performed using the R statistical computing environment.

Cell lines

The cell lines used in this study were obtained from the American Type Culture Collection in 2009 and grown under aseptic conditions in an incubator providing humidified atmosphere of 5% CO_2 in air. All cell lines were used between 3–9 passages after thawing to ensure complete revival. In addition to routine testing for mycoplasma, the identity and purity of the cell lines was validated by STR profiling. H82 and H69 cells were cultured in RPMI base media supplemented with 10% fetal bovine serum, 2 mM L-glutamine, 10 mM HEPES, 1 mM sodium pyruvate, 4,500 mg/L glucose, 1500 mg/L sodium bicarbonate and 100 U/mL penicillin and 100 μg/mL streptomycin. To facilitate the *in vivo* visualization and assessment of the growth and spread of tumor cells in orthotopic and metastatic tumor models for SCLC, H82 cells were transduced with firefly luciferase in the pLENTI6 lentiviral transfer vector (Invitrogen). After blasticidin selection, the resulting cell line, luc-H82, was used for *in vivo* bioluminescence imaging experiments. A549 cells were cultured in F-12K base media supplemented with 10% fetal bovine serum and 100 U/mL penicillin and 100 μg/mL streptomycin.

Xenograft Models

All animals were treated according to the guidelines approved by the Research Animal Resource Center and Institutional Animal Care and Use Committee at Memorial Sloan Kettering Cancer Center, NY. Four types of animal models were used in this study: (a) subcutaneous cell line xenografts; (b) orthotopic cell line xenografts; (c) subcutaneous PDX; and (d) a distant organ metastasis model. *(See SI for details)*

Synthesis of DLL3-targeting Radioimmunoconjugates

A DLL3-targeted humanized monoclonal antibody – SC16 (Stemcentrx Inc.) was chemically modified and radiolabeled with ^{89}Zr to generate a non-site-selectively modified radioimmunoconjugate (^{89}Zr-DFO-SC16-NS). A single mutation in the heavy chain of SC16 was introduced to facilitate an unpaired cysteine that could be leveraged for site-selective, maleimide-based conjugation (^{89}Zr-DFO-SC16-SS). Both antibodies were used in the PET imaging of DLL3 expression in preclinical models of SCLC. *(See SI for details)*

PET Imaging

PET imaging of the subcutaneous and orthotopic cell line xenograft mouse models of SCLC was conducted on a microPET Focus rodent scanner (Concorde Microsystems)(19), whereas PET imaging of animals in the metastatic cohort was conducted on an Inveon PET/CT scanner (Siemens). The various xenografts were administered ^{89}Zr-DFO-SC16 radioimmunoconjugates [9.25 – 11.1 MBq; (250 – 300 μCi), 31–38 μg in PBS treated with Chelex resin] via intravenous tail vein injection (t = 0). *(See SI for details)*

Biodistribution Studies

In vivo biodistribution studies were performed to evaluate the uptake of the non-site-selective versus site-selectively labeled ^{89}Zr-DFO-SC16 radioimmunoconjugates in mice bearing subcutaneous xenografts of H82, H69, A549 and PDX tumors. An isotype control radioimmunoconjugate – ^{89}Zr-DFO-hIgG-SS was injected in mice bearing subcutaneous H82 xenografts to estimate the non-specific uptake of the radioimmunoconjugate in the DLL3-positive tumor. For animals in the orthotopic xenograft and metastatic model arms of this study, a single time point biodistribution analysis was performed upon euthanizing the animals 120 h after the injection of ^{89}Zr-DFO-SC16-SS. *(See SI for details)*

Ex vivo Analyses

Subcutaneously xenografted H82, H69, Lu64, Lu149 and Lu80 tumors (n=4 per tumor type) were harvested from athymic nude mice that were not injected with any radioimmunoconjugates. Flash frozen tumor tissue was used for quantitative analyses of DLL3 expression (ng/mg of tissue) via Meso Scale Discovery (MSD) assay. Formalin-fixed, paraffin-embedded tumor tissue sections were used for immunohistochemical staining of DLL3 expression and attributed an H-Score upon analysis.

All animals (n=16) in the metastatic cohort of this study injected with ^{89}Zr-DFO-SC16-SS [7.4 MBq; (200 μCi)] for imaging via PET and bioluminescence were euthanized via CO_2(g) asphyxiation and all vital organs including the head were harvested and analyzed for biodistribution of ^{89}Zr-DFO-SC16-SS and histopathology. The read outs from the histopathological analyses were matched with the PET images to validate their anatomical correlation.

Statistical Analyses

All data presented in this study are expressed as means ± SD. Where applicable, statistical differences were analyzed by unpaired, two-tailed, Student's t-test using GraphPad Prism 7 software. Multiple comparisons with adjusted p-values <0.05 were considered statistically significant. To evaluate the various tumor-to-background tissue ratios between the two SC16-based radioimmunoconjugates, uncertainty propagation errors were used and a correction for multiple comparisons was done using the Holm-Sidak method to determine statistical significance.

RESULTS

Evaluation of DLL3 target expression in SCLC and normal tissues

To identify genes expressed in SCLC that are minimally expressed in normal tissues, we combined RNAseq data from 51 human SCLC samples and 2,712 normal samples, representing 55 different organs into a single gene expression data set. 27,195 transcripts with detectable expression in SCLC were ranked based on the scaled difference between the median SCLC reads per kilobase of transcript per million mapped reads (RPKM) and the upper quartile RPKM of the highest expressing normal tissue. The ranked gene list of 3,915 genes with higher median expression in SCLC than any normal tissue was then filtered based on gene ontology to include genes intrinsic to a membrane and exclude genes with

likely intracellular localization. Of the 60 candidate genes meeting these criteria, and confirming previous reports (7), *DLL3* had the most favorable gene expression profile, being highly expressed in SCLC with relatively lower levels in pituitary, brain, and testis (Fig. 1A). *DLL3* expression in brain tissues was greatest in nucleus accumbens with less expression in hippocampus (Fig. 1B). No single normal sample exceeded the median expression in SCLC.

Selection of cell lines for immunoPET

In order to identify appropriate cell lines for preclinical testing of a DLL3-targeted immunoPET agent, we turned to publicly available gene expression data from the Cancer Cell Line Encyclopedia (CCLE). A mining expedition of the gene expression data from cell lines in the CCLE yielded an expression cutoff between cells that did not express *DLL3*, and the 104/1,015 (10.2%) that expressed various levels of *DLL3* (Fig. 1C). Expression data for SCLC cell lines was extracted, among which, 32/53 (60.4%) expressed *DLL3*. Two *DLL3*-expressing cell lines, H82 and H69, were chosen for further analysis (Fig. 1C). H82 had median *DLL3* expression and may represent the typical expression level found in human SCLC cell lines. H69 was selected to represent the lower quartile of *DLL3*-positive SCLC cell lines in order to challenge the sensitivity limits of DLL3 immunoPET imaging. *In vitro* cell binding assays using ^{89}Zr-DFO-SC16-NS with H82, H69, and A549 cells revealed the binding of the radioimmunoconjugate to bear excellent concordance to the predicted level of DLL3 expressed by the 3 cell lines (Fig. 1D). Further, a Meso Scale Discovery (MSD) assay yielded 58.2 ng/mg, 14 ng/mg and 1 ng/mg of DLL3 expressed by H82, H69 and A549 tumors respectively. Similarly, immunohistochemistry yielded H-scores of 195, 55 and 0 respectively for the three tumors (Fig. 1F).

Characterization of the radioimmunoconjugates and target abundance

We synthesized two SC16-based immunoconjugates to evaluate as immunoPET tracers for the molecular imaging of DLL3 in preclinical models of SCLC. One of these immunoconjugates — DFO-SC16-NS — was synthesized through the random coupling of isothiocyanate-bearing DFO moieties to the lysines of the antibody, while the other — DFO-SC16-SS — was created via the site-selective conjugation of a maleimide-bearing variant of DFO with unpaired cysteine residues within the hinge region of the SC16 immunoglobulin (Fig. 2A). Mass spectrometry analysis revealed that DFO-SC16-NS had ~3.5 DFOs per antibody, with DFOs distributed between the light and heavy chains of the antibody (Figs. S1a–d). A similar analysis of DFO-SC16-SS revealed that it had 2.8 DFOs conjugated per antibody (Figs. S2a–d). Both the constructs showed ≥ 90% immunoreactive fractions as determined via surface plasmon resonance experiments (Fig. S3a–b).

Upon radiolabeling with $^{89}Zr^{4+}$, both ^{89}Zr-DFO-SC16-NS and ^{89}Zr-DFO-SC16-SS were reproducibly obtained in high radiochemical yields (>95 %) and high specific activities (7.5 – 9.0 mCi/mg). The radioimmunoconjugates were isolated in high radiochemical purity (>99%), and demonstrated ≥95% stability (^{89}Zr-DFO-SC16-NS) and 85% stability (^{89}Zr-DFO-SC16-SS) against demetallation when incubated in human serum at 37 °C over a period of 5 days (Figs. S4 and S5). Saturation ligand-binding assays performed on sections prepared from subcutaneously xenografted H82 and H69 tumors validated the nanomolar

affinity (K_D) of the ^{89}Zr-DFO-SC16-NS construct for binding to DLL3 and yielded B_{max} concentrations of 14.7 ± 0.6 nM (H82) and 6.0 ± 0.5 nM (H69) to indicate the maximum number of DLL3 sites available per cell for binding of the SC16 antibody in the respective tumors. The nanomolar B_{max} concentration was converted to numeric values based on a mean SCLC cell diameter of 10 μm, which yielded ~ 14,000 and 6,000 DLL3 molecules available per cell in H82 and H69 tumor sections respectively (Fig. 1E) (20). A comparison of this range of expression levels of DLL3 with other tumor-associated antigens that have been targeted for the immunoPET imaging of cancer revealed that DLL3 expression in SCLC was lower by *at least* 2 orders of magnitude (Fig. 1G) (21–30). Finally, although upregulated in SCLC relative to non-malignant adult cells, DLL3 is a remarkably low-abundance protein on the surface of tumor cells, having on the order of only 10,000 molecules expressed per cell. We hypothesized that immunoPET imaging might still be feasible given the near-complete absence of DLL3 cell surface expression on normal tissues.

Evaluation of SC16-based radioimmunoconjugates in subcutaneous xenograft models

In vivo PET imaging studies with the two SC16-based radioimmunoconjugates clearly delineated H82 and H69 tumors in subcutaneous xenografts (Figs. 2B–E). A higher concentration of radioactivity was found in the H82 tumors than in H69 tumors. Conversely, even 120 h after the injection of the ^{89}Zr-DFO-SC16-SS and ^{89}Zr-DFO-SC16-NS, a higher PET signal was found to persist in the systemic circulation of H69 xenografts (Figs. 2C and 2E). The *in vivo* biodistribution of the radioimmunoconjugates in subcutaneous H82 and H69 xenografts demonstrated a progressively increasing concentration of radioactivity in the tumors over time (Figs. 3A, 3D, S6–S9). The tumoral uptake values of the radioimmunoconjugates in H82 and H69 tumors corresponded well with the level of DLL3 expression in these tumors as determined via *in vitro* and *ex vivo* analyses. Specifically, ^{89}Zr-DFO-SC16-SS yielded an uptake value of 27.3 ± 6.0 %ID/g in H82 tumors, whereas the H69 tumors afforded 16.2 ± 5.8 %ID/g. Furthermore, the concentration of radioactivity in both the tumors could be blocked by the co-injection of a 100-fold excess of un-labeled SC16 antibody (Figs. 3A and 3D; Tables S1 and S2).

A comparison between the biodistribution of the site-selectively labeled versus non-site-selectively labeled SC16-based radioimmunoconjugates in H82 xenografts revealed that ^{89}Zr-DFO-SC16-SS yielded a tumor uptake of 27.3 ± 6.0 %ID/g whereas ^{89}Zr-DFO-SC16-NS afforded 19.5 ± 4.8 %ID/g (Fig. 3B; Tables S1 and S3). Notably, a higher concentration of radioactivity was observed in the kidneys of H82 xenografts injected with the site-selectively labeled construct (6.2 ± 1.1 %ID/g) than those injected with ^{89}Zr-DFO-SC16-NS (3.5 ± 0.5 %ID/g) (Fig. 3B; Tables S1 and S3). A similar trend was observed for the biodistribution of the SC16-based radioimmunoconjugates in the tumors and background tissues of H69 xenografts (Figs. 3E and S10; Tables S2 and S4). Despite the slightly higher activity concentrations of ^{89}Zr-DFO-SC16-SS in the tumors and kidneys of H82 xenografts, comparable tumor-to-background ratios were obtained for ^{89}Zr-DFO-SC16-SS versus ^{89}Zr-DFO-SC16-NS injected in H82 xenografts in most tissues except the liver, which displayed a marginally significant difference (adjusted p-value = 0.076) (Fig. 3C, Table S5). Further, an evaluation of the ratio of the tumor-to-background ratios between ^{89}Zr-DFO-SC16-SS and ^{89}Zr-DFO-SC16-NS yielded Tumor-to-Kidney$_{(SS/NS)}$ = 0.79 ± 0.31; Tumor-to-

$Liver_{(SS/NS)}$ = 2.14 ± 1.04; $Tumor\text{-}to\text{-}Blood_{(SS/NS)}$ = 1.13 ± 0.48; and $Tumor\text{-}to\text{-}Muscle_{(SS/NS)}$ = 1.36 ± 0.55. Finally, the biodistribution of ^{89}Zr-DFO-SC16-SS in subcutaneous xenografts of a DLL3-negative non-small cell lung cancer (A549) compared well with that of a site-selectively radiolabeled anti-hapten isotype-matched IgG (^{89}Zr-DFO-hIgG-SS) in DLL3-positive H82 xenografts. In both these cases, low and non-specific uptake of the radioimmunoconjugates was observed based on the *in vivo* enhanced permeability and retention effect (5–7 %ID/g at 120 h p.i.) (Figs. 3F, S11, S12; Tables S6 and S7).

These data are particularly encouraging since the SC16 antibody is known to cross-react with murine DLL3 protein (7). The observed accretion of the SC16-radioimmunoconjugates in SCLC tumors is highly specific and attributed to the tumor selective expression of human DLL3, and not due to the enhanced permeability and retention (EPR) effect in tumors or the lack of species cross-reactivity that can artificially lower the background signal in immunoPET imaging studies.

DLL3 PET imaging of orthotopic, metastatic and PDX models of SCLC

In an orthotopic model of SCLC, a high concordance was achieved between the bioluminescence signal from luc-H82 tumors engrafted in the left lung of athymic nude mice and PET imaging with ^{89}Zr-DFO-SC16-SS, which successfully delineated the lung tumors (Figs. 4A-C and S13). Analysis of the biodistribution of ^{89}Zr-DFO-SC16-SS in this model showed a highly selective concentration of radioactivity within the orthotopically xenografted left lung versus the right lung (Fig. 4D).

In a mouse model developed to mimic distant organs metastases of SCLC, PET/CT imaging with ^{89}Zr-DFO-SC16-SS followed by necropsy for biodistribution studies at 136 h after the injection of the radioimmiunoconjugate revealed a diverse set of findings. Though varying in intensity, the most prominent signal was obtained from the livers in all the mice that were examined in this cohort. Necropsy of the animals revealed the abundance of metastatic nodules to have a strong qualitative concordance with the intensity of the PET signal observed in the liver. Liver tissue with a semi-quantitative histopathological score of 2–3, yielded low intensity PET signal and had an uptake of ~10.7 ± 1.2 %ID/g as measured from biodistribution analysis. On the other hand, livers with a histopathological score of 5–6 yielded a relatively high intensity PET signal with an uptake of ~ 14 ± 1.5 %ID/g as measured in biodistribution analysis (Fig. 4K). The high intensity foci of PET signal from the liver correlated well with coalescing metastatic lesions found in the liver tissues examined via histopathology. Interestingly, 50% (8/16) of the animals in the metastatic experimental cohort showed unilateral and/or bilateral PET-positive ovaries (Figs. 4E, 4I, 4K). There was a strong correlation between findings from PET imaging, necropsy, biodistribution analysis and histopathology of the ovarian tissues. No false positives were obtained in our studies despite unilateral involvement of ovarian metastases in 37.5 % (3/8) of cases.

Among other sites of interest for metastases in our experimental cohort, 50% (8/16) of the mice showed distinct PET and bioluminescence signals within the head (Figs. 5A and 5B). Histopathologic analysis revealed a predominant infiltration of the hemimandibles (Figs. 5C

and 5D) and sporadic infiltration of the pituitary gland (Fig. S14). On the other hand, although the bone tissue was positive on PET images (Figs. 4E, S15), the regional localization of the PET signal was somewhat discordant with that of neoplastic cells found in this tissue. Furthermore, a consistently high concentration of radioactivity was seen in the spleen, which appeared strongly PET-positive (Figs. S16A, S16C) and was associated with uptake values >85 %ID/g as determined in the biodistribution analysis of all the mice within the metastatic model cohort. However, all the spleens examined were histopathologically negative for the presence of tumor cells (Fig. S16B and S16D). Interestingly, tandem injections with the same batch of the radioimmunoconjugate in female athymic nude mice did not yield high intensity splenic PET signals (Fig. S17, S18).

When injected in mice bearing subcutaneously transplanted SCLC PDX, ^{89}Zr-DFO-SC16-SS clearly delineated the PDX tumors via PET imaging (Figs. 6A–C). In biodistribution studies, Lu64 tumors, which have the highest reported DLL3 expression (4.25 ng/mg) and sensitivity to treatment with SC16LD6.5 (7), demonstrated the highest tumor uptake of ^{89}Zr-DFO-SC16-SS (67.7 ± 13.8 %ID/g) at 120 h after the injection of the radioimmunoconjugate in the present study (Figs. 6A, 6D, 6E, 6F). On the other hand, Lu149 tumors, which represented a median concentration for DLL3 expression (2.71 ng/mg), demonstrated an intermediate tumor uptake for ^{89}Zr-DFO-SC16-SS (38.1 ± 1.8 %ID/g) at 120 h after the injection of the radioimmunoconjugate (Figs. 6B, 6D, 6E, 6F). Finally, Lu80 tumors were representative of a low DLL3 expression candidate (0.6 ng/mg) and afforded the least uptake (21.2 ± 2.4 %ID/g) in the tumors at 120 h after the injection of the radioimmunoconjugate (Figs. 6C–F). Surprisingly, despite the low level of DLL3 expression in the Lu80 PDX tumors, a relatively high concentration of radioactivity was found associated with these tumors. To some extent, this may be due to perfusion from a sheath of blood that encased the subcutaneously xenografted Lu80 tumors unlike other PDXs examined in this study (Fig. S19). Notably, many tumors in the SC16LD6.5-treated cohorts of Lu80 have previously been shown to escape disease control (7).

DISCUSSION

Early phase clinical trials of Rova-T have assessed DLL3 expression from initial diagnostic biopsies by IHC. Although IHC appears to be an effective method to assess DLL3 expression status, it suffers from several practical limitations that may hinder its utility in the clinic, chief among them being the requirement for invasive research biopsies in previously treated SCLC, which may recur in inaccessible sites and for which clinical justification for re-biopsy is generally lacking.

Premised on the early success of Rova-T and the emerging role of precision medicine to improve clinical outcomes, we envisaged that a companion imaging diagnostic for this drug could potentially facilitate the identification, selection and stratification of SCLC patients for treatment with Rova-T on the basis of their *in vivo* DLL3 expression status and serve as a tool with which to monitor for recurrence or determine whether Rova-T retreatment should be an option for patients upon recurrence. A DLL3-targeted molecular imaging agent could potentially provide clinicians with real-time information about the *in vivo* expression of

DLL3 while concomitantly delineating SCLC tumors in a noninvasive whole body PET scan.

The foremost challenge to image DLL3 expression via PET lay in its low abundance on the surface of tumor cells. Syndecan-1 and HER3 are among the few other tumor-associated antigens with similar expression densities that have been targeted for the PET imaging of cancer (24, 28, 29). In our hands, although the in vivo tumor uptake of the site-selectively-labeled SC16 radioimmunoconjugate (^{89}Zr-DFO-SC16-SS) was not significantly different from its non-site-selectively-labeled cousin (^{89}Zr-DFO-SC16-NS), ^{89}Zr-DFO-SC16-SS represented a biochemically site-selective and functionally active radioimmunoconjugate that yielded favorable in vivo tumor-to-background ratios that might be further improved.

Among the chosen SCLC cell line tumors, the relatively low target sink provided by the H69 tumors resulted in a higher concentration of radioactivity to persist within the systemic circulation of H69 tumor-bearing mice even 120 h after the injection of the radioimmunoconjugates. This observation may be critical to the dosing of patients with the Rova-T ADC and/or potential targeted-radiotherapy with ^{177}Lu/^{90}Y-labeled SC16 antibody, wherein patients with lesser tumor burden or lower *in vivo* tumoral expression of DLL3 are more likely to have an excess of the "*targeted*" drug lingering within the systemic circulation. In such patients, adjusted dosing of the DLL3-targeted ADC or radioimmunotherapeutic agent may be warranted to avoid treatment-related toxicities.

Finally, a critical benchmark that defines the clinical utility of immunoPET tracers lies in their ability to predict response to therapy based on in vivo imaging. In this context, ^{89}Zr-DFO-SC16-SS demonstrated rank order correlation in clinically representative PDX models of SCLC with previously documented responses to therapy with SC16LD6.5. Furthermore, the ability of ^{89}Zr-DFO-SC16-SS to noninvasively delineate micrometastatic foci with high sensitivity may potentially translate into the clinical detection of distant organ micrometastatic lesions in patients. Metastases to the brain are a common finding in SCLC patients and cannot be detected via ^{18}F-FDG-PET due to the background caused by high uptake of glucose in the brain. The PET imaging performance of ^{89}Zr-labeled Trastuzumab in the clinic encourages us to speculate that DLL3 immunoPET could potentially enable the identification of metastatic lesions in the brain of SCLC patients (31). Furthermore, our findings of the multinodular infiltration pattern in the ovaries of mice within the metastatic cohort were consistent with clinical reports of metastatic SCLC found in the ovaries of human patients (32). Sparing of the ovarian surface epithelium and bursa in all the cases that were examined is indicative of the hematogenous spread of the disease to the ovary. Although metastases to the mandible and alveolar bone is seldom observed in human patients, in our preclinical model the premolar–molar region may be providing an ideal site for metastatic seeding due to a predominance of red bone marrow and retardation of the circulation in this anatomic location.

Despite the excellent *in vivo* performance of ^{89}Zr-DFO-SC16-SS as a DLL3 PET imaging agent, our experiments highlighted some limitations of the immunoPET agent and the preclinical models that were used for its evaluation. Most importantly, the chelator-to-antibody ratio (CAR = 1–4) for the site-selectively labeled ^{89}Zr-DFO-SC16-SS construct

used for PET imaging experiments differs from the drug-to-antibody ratio (DAR = 2) for the Rova-T construct used in clinical trials. This may be a result of a stronger reduction of the inter-chain disulfide bonds in the SC16 antibody with a 10-fold molar excess of TCEP used for the synthesis of ^{89}Zr-DFO-SC16-SS compared to the 1–2 fold molar excess of the mild-reducing agent used in the synthesis of SC16LD6.5 (7). In our case, a high CAR was desirable in order to yield a high specific activity immunoPET imaging agent that retains target binding capability and can delineate the expression of a low abundance tumor specific target such as DLL3.

Arguably, the elevated concentration of radioactivity in the kidneys of xenografts injected with ^{89}Zr-DFO-SC16-SS may be attributed to the labile nature of the thiol-maleimide linkage for *in vivo* hydrolysis. This is exacerbated by the tendency of the thioether bond to undergo retro-Michael addition reactions in the presence of reactive thiols of serum proteins such as albumin and/or free cysteines and glutathione present in the kidneys (33). Through this mechanism, the macrocylic chelator and the ^{89}Zr encased within it could be dissociated from the antibody and be systemically cleared through the kidneys. More stable thiol-reactive methylsufonyl-functionalized heteroaromatic linkers may improve the stability of the immunoconjugate (34). Another limitation revealed by immunoPET imaging with ^{89}Zr-DFO-SC16-SS in the metastatic SCLC model was the PET signal observed in the bone and the spleen, which had discordant histopathologic read outs for the presence of metastases in these tissues. These observations may most likely be related to the biology of the immunocompromised NSG mouse strain.

In conclusion, the work at hand describes the thorough preclinical evaluation of a DLL3-targeted companion diagnostic agent for potential use in the clinic. Such a tracer can noninvasively provide real-time information about the status of *in vivo* DLL3 expression and delineate the presence of SCLC tumors to facilitate the selection of patients for treatment with a therapeutic counterpart such as Rova-T and other DLL3-targeted therapeutics. Additionally, several salient features related to the development of immunoPET tracers and preclinical animal models were highlighted through the experiments undertaken in this study. First, our study demonstrates that low abundance tumor-associated molecular targets/antigens such as DLL3 can be targeted for PET imaging, provided the target is unique to neoplastic cells and its *in vivo* expression in background tissues is minimal. Next, our study illustrates a comparative evaluation of using site-selectively modified immunoconjugates over their non-site-selectively modified cousins for applications related to the targeted imaging and therapy of cancer. In this context, the critical role and limitations of the chemistry used in the preparation of such immunoconjugates was highlighted. Finally, the DLL3 PET imaging agent ^{89}Zr-DFO-SC16-SS consistently demonstrated highly sensitive and selective targeting of DLL3 to delineate SCLC tumors *in vivo* in a host of preclinical mouse models.

Supplementary Material

Refer to Web version on PubMed Central for supplementary material.

Acknowledgments

Financial Support: This work was supported by a grant from the Druckenmiller Center for Lung Cancer Research (J.T. Poirier, J.S. Lewis) and NIH grants U01 CA213359 (J.T. Poirier, J.S. Lewis) and R01 CA213448 (J.T. Poirier, J.S. Lewis, C.M. Rudin). This work was made possible by using the MSKCC Small Animal Imaging Core Facility, the Radiochemistry and Molecular Imaging Probe core, the Anti-tumor Assessment Core, and the Tri-Institutional Laboratory of Comparative Pathology, which were supported in part by NIH grant P30 CA08748.

References

1. Bunn PA Jr, Minna JD, Augustyn A, Gazdar AF, Ouadah Y, Krasnow MA, et al. Small Cell Lung Cancer: Can Recent Advances in Biology and Molecular Biology Be Translated into Improved Outcomes? J Thorac Oncol. 2016; 11:453–74. [PubMed: 26829312]
2. Siegel RL, Miller KD, Jemal A. Cancer statistics, 2016. CA Cancer J Clin. 2016; 66:7–30. [PubMed: 26742998]
3. Miller KD, Siegel RL, Lin CC, Mariotto AB, Kramer JL, Rowland JH, et al. Cancer treatment and survivorship statistics, 2016. CA Cancer J Clin. 2016; 66:271–89. [PubMed: 27253694]
4. Joshi M, Ayoola A, Belani CP. Small-cell lung cancer: an update on targeted therapies. Adv Exp Med Biol. 2013; 779:385–404. [PubMed: 23288650]
5. Rekhtman N. Neuroendocrine tumors of the lung: an update. Arch Pathol Lab Med. 2010; 134:1628–38. [PubMed: 21043816]
6. Oze I, Hotta K, Kiura K, Ochi N, Takigawa N, Fujiwara Y, et al. Twenty-seven years of phase III trials for patients with extensive disease small-cell lung cancer: disappointing results. PLoS One. 2009; 4:e7835. [PubMed: 19915681]
7. Saunders LR, Bankovich AJ, Anderson WC, Aujay MA, Bheddah S, Black K, et al. A DLL3-targeted antibody-drug conjugate eradicates high-grade pulmonary neuroendocrine tumor-initiating cells in vivo. Sci Transl Med. 2015; 7:302ra136.
8. Geffers I, Serth K, Chapman G, Jaekel R, Schuster-Gossler K, Cordes R, et al. Divergent functions and distinct localization of the Notch ligands DLL1 and DLL3 in vivo. J Cell Biol. 2007; 178:465–76. [PubMed: 17664336]
9. Hann CL, Rudin CM. Fast, hungry and unstable: finding the Achilles' heel of small-cell lung cancer. Trends Mol Med. 2007; 13:150–7. [PubMed: 17324626]
10. Dylla SJ. Toppling high-grade pulmonary neuroendocrine tumors with a DLL3-targeted trojan horse. Mol Cell Oncol. 2016; 3:e1101515. [PubMed: 27308627]
11. Rudin CM, Pietanza MC, Bauer TM, Ready PN, Morgensztern D, Glisson PBS, et al. An openlabel study of rovalpituzumab tesirine (SC16LD6.5), a delta-like protein 3-targeted antibody-drug conjugate, in recurrent small cell lung cancer. Lancet Oncology. In Press.
12. Wu AM. Antibodies and antimatter: the resurgence of immuno-PET. J Nucl Med. 2009; 50:2–5. [PubMed: 19091888]
13. Jauw YW, Menke-van der Houven van Oordt CW, Hoekstra OS, Hendrikse NH, Vugts DJ, Zijlstra JM, et al. Immuno-Positron Emission Tomography with Zirconium-89-Labeled Monoclonal Antibodies in Oncology: What Can We Learn from Initial Clinical Trials? Front Pharmacol. 2016; 7:131. [PubMed: 27252651]
14. Pandit-Taskar N, O'Donoghue JA, Durack JC, Lyashchenko SK, Cheal SM, Beylergil V, et al. A Phase I/II Study for Analytic Validation of 89Zr-J591 ImmunoPET as a Molecular Imaging Agent for Metastatic Prostate Cancer. Clin Cancer Res. 2015; 21:5277–85. [PubMed: 26175541]
15. Ulaner GA, Hyman D, Ross D, Corben A, Chandarlapaty S, Goldfarb S, et al. Detection of HER2-positive metastases in patients with HER2-negative primary breast cancer using the 89Zr-DFO-trastuzumab PET/CT. J Nucl Med. 2016
16. Knowles SM, Wu AM. Advances in immuno-positron emission tomography: antibodies for molecular imaging in oncology. J Clin Oncol. 2012; 30:3884–92. [PubMed: 22987087]
17. Ritchie ME, Phipson B, Wu D, Hu Y, Law CW, Shi W, et al. limma powers differential expression analyses for RNA-sequencing and microarray studies. Nucleic Acids Res. 2015; 43:e47. [PubMed: 25605792]

18. Zilliox MJ, Irizarry RA. A gene expression bar code for microarray data. Nat Methods. 2007; 4:911–3. [PubMed: 17906632]
19. Tai YC, Ruangma A, Rowland D, Siegel S, Newport DF, Chow PL, et al. Performance evaluation of the microPET focus: a third-generation microPET scanner dedicated to animal imaging. J Nucl Med. 2005; 46:455–63. [PubMed: 15750159]
20. Lee TK, Esinhart JD, Blackburn LD, Silverman JF. The size of small cell lung carcinoma cells. Ratio to lymphocytes and correlation with specimen size and crush artifact. Anal Quant Cytol Histol. 1992; 14:32–4. [PubMed: 1313679]
21. Kurai J, Chikumi H, Hashimoto K, Yamaguchi K, Yamasaki A, Sako T, et al. Antibody-dependent cellular cytotoxicity mediated by cetuximab against lung cancer cell lines. Clin Cancer Res. 2007; 13:1552–61. [PubMed: 17332301]
22. Lewis Phillips GD, Li G, Dugger DL, Crocker LM, Parsons KL, Mai E, et al. Targeting HER2-positive breast cancer with trastuzumab-DM1, an antibody-cytotoxic drug conjugate. Cancer Res. 2008; 68:9280–90. [PubMed: 19010901]
23. Li C, Chacko AM, Hu J, Hasegawa K, Swails J, Grasso L, et al. Antibody-based tumor vascular theranostics targeting endosialin/TEM1 in a new mouse tumor vascular model. Cancer Biol Ther. 2014; 15:443–51. [PubMed: 24553243]
24. Mirschberger C, Schiller CB, Schraml M, Dimoudis N, Friess T, Gerdes CA, et al. RG7116, a therapeutic antibody that binds the inactive HER3 receptor and is optimized for immune effector activation. Cancer Res. 2013; 73:5183–94. [PubMed: 23780344]
25. Nakajima T, Mitsunaga M, Bander NH, Heston WD, Choyke PL, Kobayashi H. Targeted, activatable, in vivo fluorescence imaging of prostate-specific membrane antigen (PSMA) positive tumors using the quenched humanized J591 antibody-indocyanine green (ICG) conjugate. Bioconjug Chem. 2011; 22:1700–5. [PubMed: 21740058]
26. Nestor M, Ekberg T, Dring J, van Dongen GA, Wester K, Tolmachev V, et al. Quantification of CD44v6 and EGFR expression in head and neck squamous cell carcinomas using a single-dose radioimmunoassay. Tumour Biol. 2007; 28:253–63. [PubMed: 17992053]
27. Repetto-Llamazares AH, Larsen RH, Patzke S, Fleten KG, Didierlaurent D, Pichard A, et al. Targeted Cancer Therapy with a Novel Anti-CD37 Beta-Particle Emitting Radioimmunoconjugate for Treatment of Non-Hodgkin Lymphoma. PLoS One. 2015; 10:e0128816. [PubMed: 26066655]
28. Rousseau C, Ruellan AL, Bernardeau K, Kraeber-Bodere F, Gouard S, Loussouarn D, et al. Syndecan-1 antigen, a promising new target for triple-negative breast cancer immuno-PET and radioimmunotherapy. A preclinical study on MDA-MB-468 xenograft tumors. EJNMMI Res. 2011; 1:20. [PubMed: 22214534]
29. Yuan Q, Furukawa T, Tashiro T, Okita K, Jin ZH, Aung W, et al. Immuno-PET Imaging of HER3 in a Model in which HER3 Signaling Plays a Critical Role. PLoS One. 2015; 10:e0143076. [PubMed: 26571416]
30. Berk DA, Yuan F, Leunig M, Jain RK. Direct in vivo measurement of targeted binding in a human tumor xenograft. Proc Natl Acad Sci U S A. 1997; 94:1785–90. [PubMed: 9050856]
31. Dijkers EC, Oude Munnink TH, Kosterink JG, Brouwers AH, Jager PL, de Jong JR, et al. Biodistribution of 89Zr-trastuzumab and PET imaging of HER2-positive lesions in patients with metastatic breast cancer. Clin Pharmacol Ther. 2010; 87:586–92. [PubMed: 20357763]
32. Irving JA, Young RH. Lung carcinoma metastatic to the ovary: a clinicopathologic study of 32 cases emphasizing their morphologic spectrum and problems in differential diagnosis. Am J Surg Pathol. 2005; 29:997–1006. [PubMed: 16006793]
33. Patterson JT, Asano S, Li X, Rader C, Barbas CF 3rd. Improving the serum stability of site-specific antibody conjugates with sulfone linkers. Bioconjug Chem. 2014; 25:1402–7. [PubMed: 25099687]
34. Toda N, Asano S, Barbas CF 3rd. Rapid, stable, chemoselective labeling of thiols with Julia-Kocienski-like reagents: a serum-stable alternative to maleimide-based protein conjugation. Angew Chem Int Ed Engl. 2013; 52:12592–6. [PubMed: 24123851]

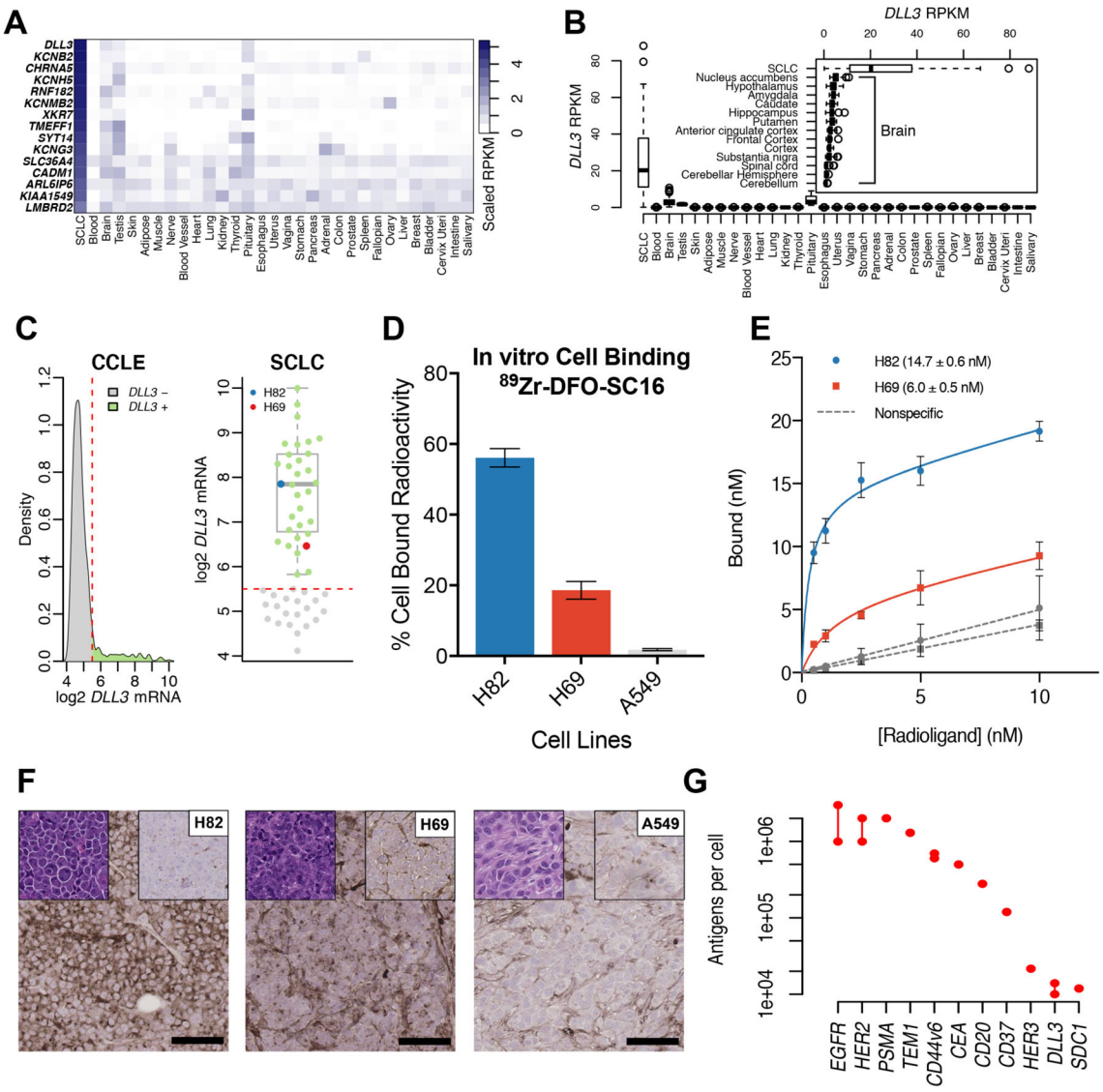

Figure 1. DLL3 is a unique low-abundance cell surface target expressed in small cell lung cancer

(A) A heat map comparing the median RPKM of cell surface proteins elevated in small cell lung cancer (SCLC) to the median RPKM in normal adult tissues. *DLL3* has abundant expression in SCLC and minimal expression in normal tissues with the exception of the pituitary gland, brain and testis; **(B)** A box plot comparing the median RPKM of *DLL3* in SCLC versus normal adult tissues. The inset compares the median expression of DLL3 in SCLC with different tissues of the adult brain, showing maximum expression in the nucleus accumbens; **(C)** A density plot representing the gene expression data mined for *DLL3* expression in cell lines from the Cancer Cell Line Encyclopedia (CCLE). The kernel density on the y-axis represents the cell lines that express *DLL3* in levels corresponding to values shown on the x-axis (*left*); A representation of the density plot after selection for SCLC cells alone (*right*). Two cell lines – H82 (representing the median of DLL3 expression) and H69 (low DLL3 expression < 25th percentile) were selected for the development of *in vitro* and *in vivo* experimental models described in this study; **(D)** A graph representing the differential

in vitro binding of ^{89}Zr-DFO-SC16-NS to H82, H69 and A549 cells, showing cell bound radioactivity (y-axis) in concordance with the level of DLL3 expression in the cell lines; **(E)** A plot of the saturation binding curves derived from the *ex vivo* binding of ^{89}Zr-DFO-SC16-NS to sections of H82 and H69 tumor tissue harvested from subcutaneous xenografts in mice. The curves yielded B_{max} (maximum number of DLL3 target binding sites for SC16 antibody) on the tumors; **(F)** Immunohistochemistry on subcutaneous tumor xenografts. H82 showed high DLL3 expression ~ 95% of tumor, H69 showed low DLL3 expression ~ 45% of tumor and A549 showed no DLL3 expression. Left top corner inset: H&E, Right top corner inset: isotype control, Right low corner: scale bar for 100μm **(G)** A dot plot comparing the average level of expression (protein per cell) of DLL3 with other tumor-associated molecular targets/antigens that have been used for the immunoPET imaging of various cancers.

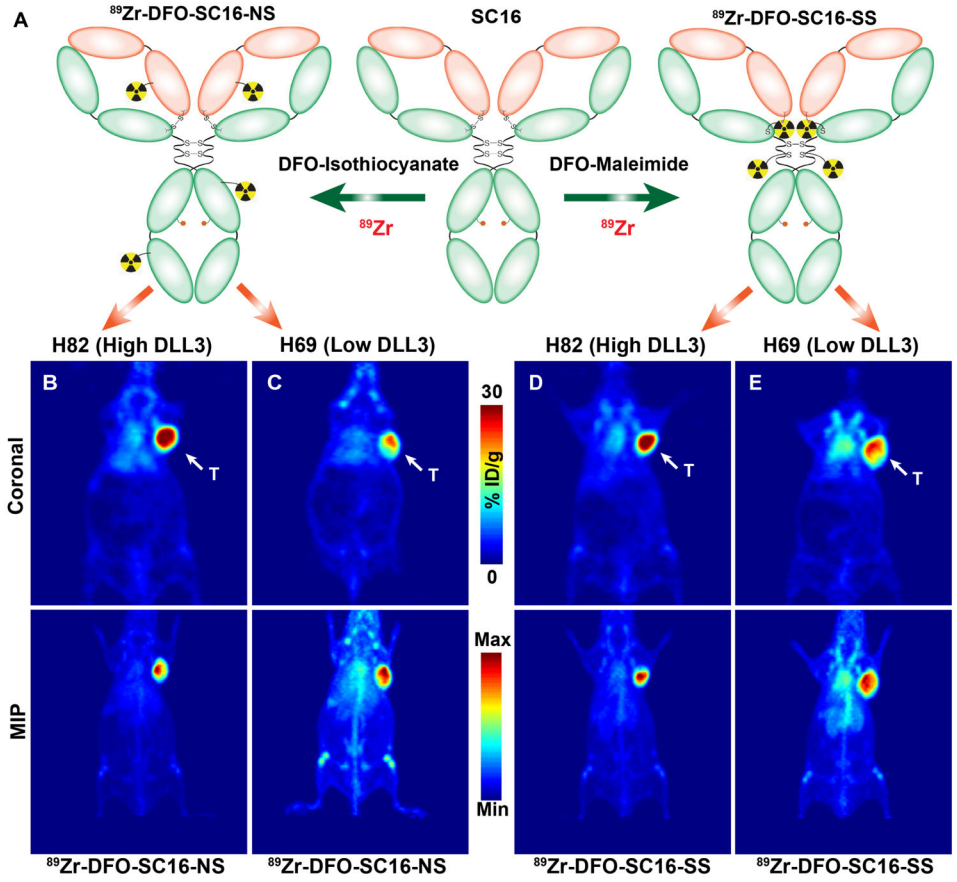

Figure 2. PET Imaging of small cell lung cancer in subcutaneous xenograft models

(A) A schematic showing the biochemical modification of the DLL3-targeted SC16 antibody with desferrioxamine (DFO) via non-site-selective conjugation (left) at randomly distributed lysine residues within the antibody to yield ^{89}Zr-DFO-SC16-NS; and via site-selective conjugation (right) at unpaired cysteine residues within the hinge region of a reduced form of the antibody to yield ^{89}Zr-DFO-SC16-SS. Representative whole body PET images – coronal slices (upper panel), Maximum Intensity Projections – MIP (lower panel) delineating the tumors via uptake of **(B)** ^{89}Zr-DFO-SC16-NS in H82 xenograft; **(C)** ^{89}Zr-DFO-SC16-NS in H69 xenograft; **(D)** ^{89}Zr-DFO-SC16-SS in H82 xenograft; and **(E)** ^{89}Zr-DFO-SC16-SS in H69 xenograft; T = tumor. The PET scans were performed at 120 h after the administration of the ^{89}Zr-labeled radioimmunoconjugates [9.25 – 11.1 MBq; (250 – 300 μCi), 31–38 μg in chelex-treated PBS] via lateral tail vein injections. Serial PET images (24 h – 120 h) for these animals are shown in Figs. S6–S9.

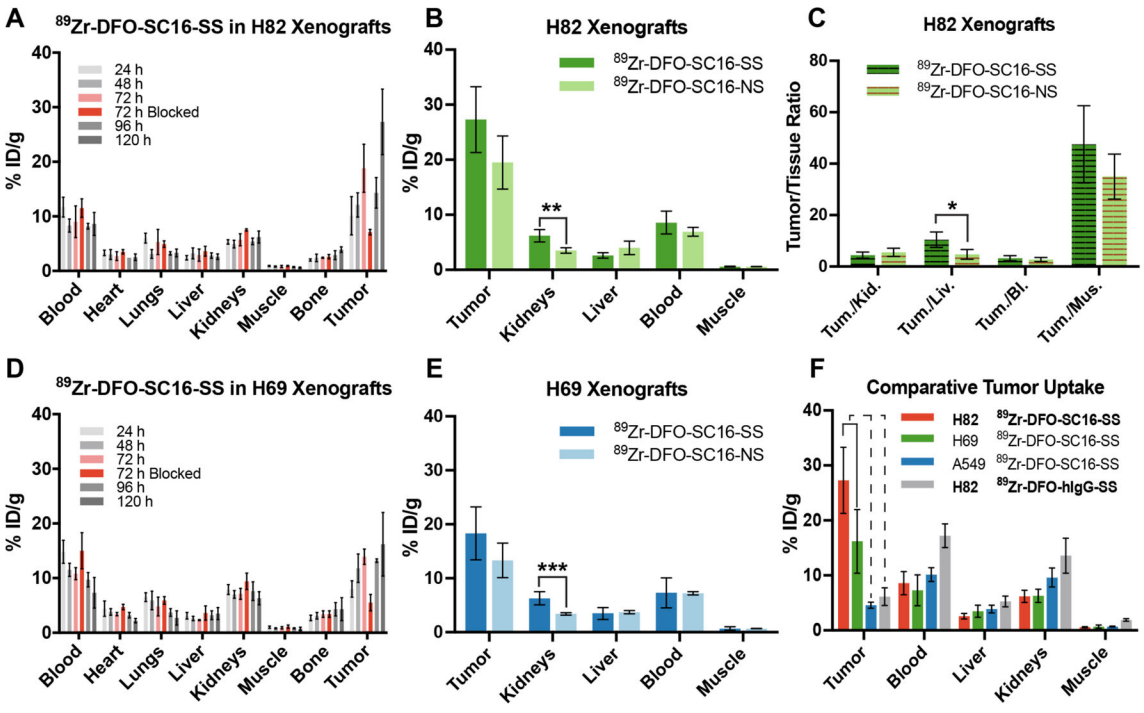

Figure 3. Biodistribution of ^{89}Zr-DFO-SC16 radioimmunoconjugates in subcutaneous xenograft models of SCLC

(A) Biodistribution data from H82 xenograft bearing mice (n = 4 per time point) after the administration of ^{89}Zr-DFO-SC16-SS via lateral tail vein injection [0.74–0.925 MBq; (20–25 μCi), 2.5–3 μg in 200 μL chelex-treated PBS]. The tumoral uptake of ^{89}Zr-DFO-SC16-SS could be blocked at 72 h by the co-injection of a 100-fold excess of the unlabeled SC16 antibody; **(B)** A graph comparing the uptake of the site-selectively labeled radioimmunoconjugate (^{89}Zr-DFO-SC16-SS) and its non-site-selectively labeled cousin (^{89}Zr-DFO-SC16-NS) at 120 h after the injection of the radioimmunoconjugates in H82 xenograft bearing mice. A higher concentration of radioactivity was found in the kidneys of xenografts injected with ^{89}Zr-DFO-SC16-SS (** indicates *adjusted p-value = 0.02*). %ID/g values are shown in tables S1 and S3; **(C)** A comparative plot of the tumor-to-background tissue ratios derived from the uptake of ^{89}Zr-DFO-SC16-SS and ^{89}Zr-DFO-SC16-NS in H82 xenograft bearing mice. Marginally higher tumor-to-background activity concentration ratios were found for ^{89}Zr-DFO-SC16-SS in the liver (* indicates *adjusted p-value = 0.076*); **(D)** Biodistribution data from H69 xenograft bearing mice (n = 4 per time point) after the administration of ^{89}Zr-DFO-SC16-NS via lateral tail vein injection [0.81–1.1 MBq; (22–30 μCi), 2.75–3.75 μg in 200 μL chelex-treated PBS). The tumoral uptake of ^{89}Zr-DFO-SC16-NS could be blocked at 72 h by the co-injection of a 100-fold excess of the unlabeled SC16 antibody; **(E)** A graph comparing the uptake of ^{89}Zr-DFO-SC16-SS and ^{89}Zr-DFO-SC16-NS at 120 h after the injection of the radioimmunoconjugates in H69 xenograft bearing mice. A higher concentration of radioactivity was found in the kidneys (*** indicates *adjusted p value = 0.015*) of xenografts injected with ^{89}Zr-DFO-SC16-SS. %ID/g values are shown in tables S2 and S4; **(F)** A summarized comparison of the uptake of ^{89}Zr-DFO-SC16-SS in subcutaneously xenografted DLL3-positive H82 and H69 tumors versus DLL3-

negative A549 tumors. The tumoral uptake of ^{89}Zr-DFO-SC16-SS was concordant with the level of DLL3 expression in the three tumors. The uptake of the ^{89}Zr-DFO-SC16-SS in A549 tumors compared well with the uptake of an isotype-matched anti-hapten radioimmunoconjugate in DLL3-posiitve H82 tumors.

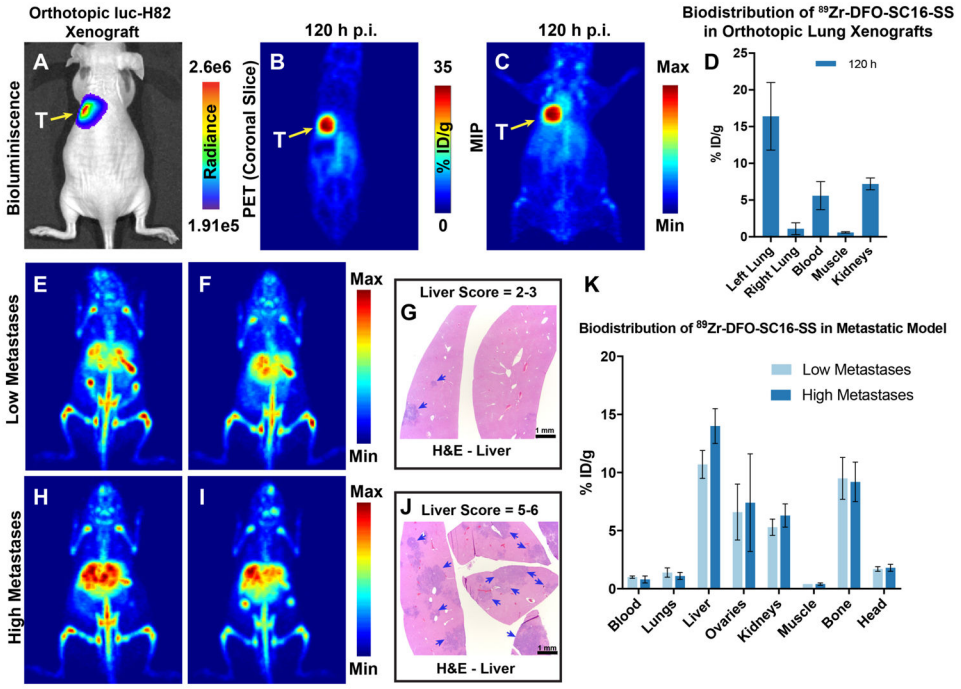

Figure 4. DLL3 PET imaging in orthotopic and metastatic models of SCLC

(A) Bioluminescence image of an athymic nude mouse bearing a luc-H82 tumor xenografted orthotopically in the left lung (yellow arrow). Radiance = photons/sec/cm^2/steradian; **(B–C)** PET images (coronal slice and MIP) of ^{89}Zr-DFO-SC16-SS delineating the orthotopically xenografted tumor (seen via bioluminescence in A). **(D)** Biodistribution of ^{89}Zr-DFO-SC16-SS in athymic nude mice bearing orthotopic xenografts of luc-H82 tumors in the left lung. A highly selective uptake was observed in the left lungs of mice, with some concentration of radioactivity found in the blood and kidneys as seen in the PET images; **(E–F)** PET images (MIPs) of 2 representative mice 136 h after the injection of ^{89}Zr-DFO-SC16-SS [7.4 MBq; (200 μCi) in 200 μL chelex-treated PBS] via the lateral tail vein. 9/16 mice in the metastatic cohort showed this pattern of low intensity focal PET signals in the liver; **(G)** H&E-stained sections of the liver lobes from mouse shown in A. Presence of small metastatic nodules (50 μm – 1 mm) (blue arrows) were seen with up to 30 % of the liver parenchyma being effaced. Mice with similar results from DLL3 PET imaging with ^{89}Zr-DFO-SC16-SS and histopathology of livers were assigned a semi-quantitative score of 2–3 and classified as having low metastatic burden. **(H–I)** PET images (MIPs) of 2 representative mice 136 h after the injection of ^{89}Zr-DFO-SC16-SS [7.4 MBq; (200 μCi) in 200 μL chelex-treated PBS] via the lateral tail vein. 7/16 mice in the metastatic cohort showed this pattern of high intensity focal PET signals in the liver; **(J)** H&E-stained sections of the liver from mouse shown in H. Presence of multiple small to large coalescing metastatic nodules (50 μm – 3 mm) (blue arrows) were seen with > 50 % of the liver parenchyma being effaced by neoplastic cells. Mice with similar results from DLL3 PET imaging with ^{89}Zr-DFO-SC16-SS and histopathology of livers were assigned a semi-quantitative score of 5–6 and classified as having high metastatic burden; **(K)** Biodistribution data from the cohort of 16 mice analyzed

for metastases via DLL3 PET. The concentration of radioactivity in the livers correlated well with the tumor burden found in these tissues.

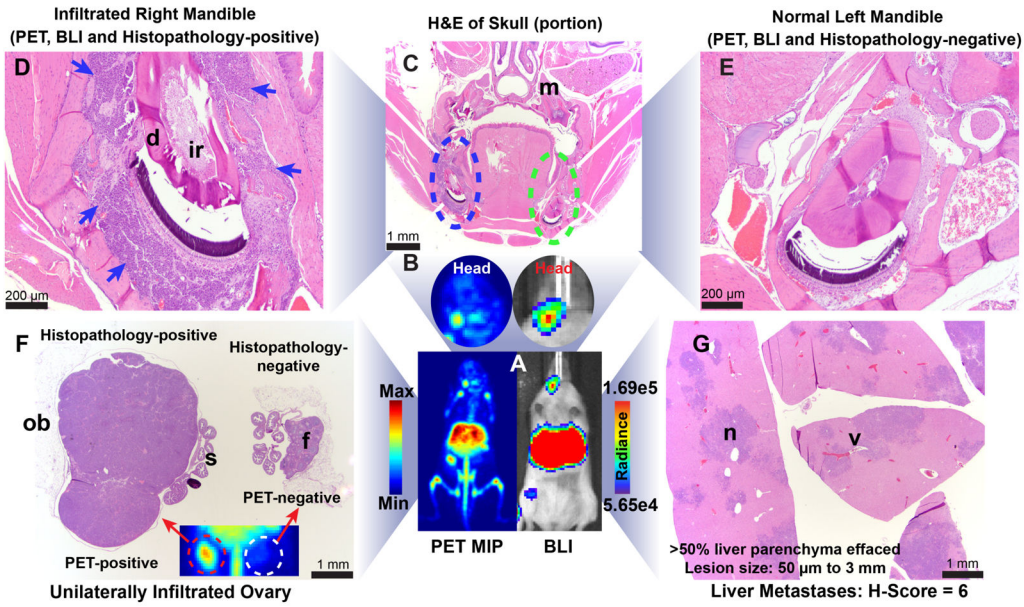

Figure 5. Concordance between DLL3 PET imaging and histopathology in a metastatic model of SCLC

(A) A side-by-side ventral view of the PET and BLI (bioluminescence) images of a representative mouse showing concordance of signals obtained from the liver and head of the mouse; **(B)** A magnified view of the head region from the PET and BLI images of the mouse showing signals localized around the right mandible of the mouse; **(C)** A coronal overview of an H&E-stained section of the decalcified skull showing infiltration of the right mandible at the level of the molars (m). Even at low magnification, the localization of neoplastic cells within the right hemimandible (blue dashed ellipse) is evident and consistent with the signals observed in the PET image and focally high luminescence observed in the BLI image; **(D)** A magnified view of the right mandible. The blue arrows point to the neoplastic cells that infiltrated and replaced most of the alveolar bone around the incisors root (ir). The dentin (d) of the tooth was intact; **(E)** A magnified view of the left hemimandible, which was devoid of neoplastic cells, confirming the lack of signal in the PET scan and BLI image; **(F)** An H&E-stained section of the two ovaries of the mouse shown in A. The ovary on the left of the image is massively enlarged due to metastatic invasion by the tumor cells. However, the salpinx (s) and the ovarian bursa (ob) were spared from neoplastic infiltration. The contralateral ovary appeared normal in size and showed the presence of immature follicles (f), which were visible within the organ. The inset shows a portion of the lower abdomen from the PET image, wherein the unilateral PET-positive ovary is seen corresponding to the histopathological findings; **(G)** H&E-stained sections of the liver from the mouse shown in A. Multiple coalescing neoplastic nodules (n) were found within the liver lobes and tend to replace more than 50% of the liver parenchyma. The multifocal and coalescing pattern of the nodules appear as multiple high intensity signals in the PET MIP. The perivascular localization (v) of metastases was a consistent finding in H&E-stained sections of all the liver tissues examined from animals in the metastatic cohort.

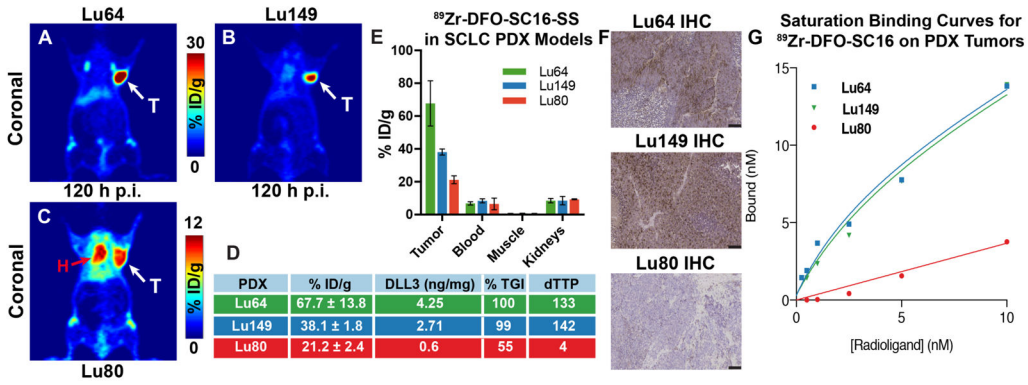

Figure 6. Rank order correlation of DLL3 PET for response to therapy with SC16LD6.5 in flank PDX models of SCLC

PET images of ^{89}Zr-DFO-SC16-SS in athymic nude mice bearing PDX – **(A)** Lu64 (high DLL3 expression); **(B)** Lu149 (medium DLL3 expression); and **(C)** Lu80 (low DLL3 expression). White arrows (A–C) point to the subcutaneously xenografted PDX tumors seen in the PET images. Red arrow (C) points to the heart and is indicative of radioactivity persisting within systemic circulation, due to the lack of a target sink in the Lu80 tumors; **(D)** A tabulated representation of the concordance between the uptake of ^{89}Zr-DFO-SC16-SS in the three PDX lines with their levels of DLL3 expression, and parameters to indicate response to therapy – %TGI (percentage tumor growth inhibition upon treatment with the antibody drug conjugate – SC16LD6.5) and dTTP (delta time to progression) for the PDX tumors after treatment with SC16LD6.5; **(E)** Biodistribution of ^{89}Zr-DFO-SC16-SS in select tissues examined from the PDX tumor bearing mice (n=4 per PDX line); **(F)** Immunohistochemistry on PDX tumors for DLL3 expression. Lu64 showed high DLL3 expression, Lu149 showed medium DLL3 expression and Lu80 showed minimal DLL3 expression. Right low corner: scale bar for 100μm. **(G)** A plot of the saturation binding curves derived from the *ex vivo* binding of ^{89}Zr-DFO-SC16-NS to sections of Lu64, Lu149 and Lu80 tumor tissue harvested from subcutaneous xenografts in mice. The curves enabled the estimation of the maximum number of DLL3 target binding sites on the PDX tumors. Lu64 had ~9400 binding sites and Lu149 had 8600 binding sites. Lu80 had negligible DLL3 expression – too low to be determined by the assay.